PCCP

Scaling analyses for hyperpolarization transfer across a spin-diffusion barrier and into bulk solid media

Journal:	*Physical Chemistry Chemical Physics*
Manuscript ID	CP-ART-06-2020-003195.R1
Article Type:	Paper
Date Submitted by the Author:	01-Dec-2020
Complete List of Authors:	Prisco, Nathan; University of California Santa Barbara, Chemical Engineering Pinon, Arthur; Ecole Polytechnique Federale de Lausanne Emsley, Lyndon; Ecole Polytechnique Fédérale de Lausanne (EPFL), Institut des Sciences et Ingénierie Chimiques Chmelka, Bradley; University of California, Santa Barbara, Department of Chemical Engineering

Scaling analyses for hyperpolarization transfer across a spin-diffusion barrier and into bulk solid media

Nathan A. Prisco,[a] Arthur C. Pinon,[b] Lyndon Emsley,[b] and Bradley F. Chmelka[a]*

By analogy to heat and mass transfer film theory, a general approach is introduced for determining hyperpolarization transfer rates between dilute electron spins and a surrounding nuclear ensemble. These analyses provide new quantitative relationships for understanding, predicting, and optimizing the effectiveness of hyperpolarization protocols, such as Dynamic Nuclear Polarization (DNP) under magic-angle spinning conditions. An empirical DNP polarization-transfer coefficient is measured as a function of the bulk matrix ^{1}H spin density and indicates the presence of two distinct kinetic regimes associated with different rate-limiting polarization transfer phenomena. Dimensional property relationships are derived and used to evaluate the competitive rates of spin polarization generation, propagation, and dissipation that govern hyperpolarization transfer between large coupled spin ensembles. The quantitative analyses agree closely with experimental measurements for the accumulation, propagation, and dissipation of hyperpolarization in solids and provide evidence for kinetically-limited transfer associated with a spin-diffusion barrier. The results and classical approach yield general design criteria for analyzing and optimizing polarization transfer processes involving complex interfaces and composite media for applications in materials science, physical chemistry and nuclear spintronics.

1. Introduction

In coupled energy transfer and dissipation processes, dimensional property analyses provide bases for understanding complex phenomena in large systems ranging from industrial-scale process equipment[1] to complex micromechanical systems.[2] Extending such constitutive analyses to the propagation of spin polarization is important for emerging applications of hyperpolarized magnetic resonance[3–7] and processes based on spin transport over multiple length scales.[8,9] In quantum computing, the coupling of electron qubits with highly polarized nuclear spin packets (*e.g.*, nuclear spintronics) is a promising strategy for extending coherence lifetimes and for facilitating short-term data storage functions.[10,11] Another example is dynamic nuclear polarization (DNP), which exploits the coupling of electron-nuclear spin ensembles to enhance dramatically NMR signal sensitivity in solids.[12] Quantitative models of DNP polarization transfer, however, have been challenging to implement,[13,14] as the generation, propagation, and dissipation of hyperpolarization can span time scales ranging from 10^{-9} to 10^{5} s, length scales from <1 nm to μm, and involve considerations of both quantum mechanical and classical phenomena. Materials systems on which these examples are based share key features, specifically complex and poorly defined interfaces between the electron spin(s) and surrounding nuclear ensemble.[15] Here, we show that the transfer of net nuclear magnetization (*i.e.*, spin polarization) from dilute paramagnetic centers to a surrounding nuclear spin ensemble exhibits fundamental similarities to thermal energy transfer and to charge transport, but importantly combines distinct aspects of both. A general model is derived for meso-scale (1–100 nm) spin transport phenomena that enables rate-limiting processes to be identified and quantitative prediction of hyperpolarization performance. The resulting insights provide criteria to guide the selection of material properties and conditions to exploit the enhanced sensitivity of hyperpolarization for diverse applications in materials science, biology and medicine, and quantum information processing.

Recent advancements in magic-angle spinning (MAS) DNP-NMR spectroscopy enable large polarization gradients to be generated near paramagnetic centers. In DNP, unpaired electron spins (*e.g.*, on dilute nitroxide biradicals) are partially saturated by microwave irradiation, resulting in hyperfine transfer to nearby nuclear spins.[12] A limitation inherent to DNP is that hyperpolarization emanates from paramagnetic centers that also impede ^{1}H–^{1}H spin diffusion, resulting in a spin-diffusion barrier.[15–18] Many fundamental insights have been obtained from quantum-mechanical treatments that have elucidated the cross-effect mechanism and hyperpolarization transfer at different magnetic fields or MAS rates.[18–21] While these approaches have been extended to realistically large spin systems,[22,23] it remains challenging to quantitatively predict hyperpolarization transfer rates to distant ^{1}H nuclei, particularly across the spin-diffusion barrier (Fig. 1a) and across interfaces (Fig. 1b). Here, scaling analyses are used to generalize spin transport phenomena, elucidate rate-limiting processes, and identify conditions for which classical thermodynamic models[24] can accurately reproduce spin polarization transfer kinetics. The approach yields dimensionless parameters that provide quantitative insights and criteria which allow polarization build-up rates and enhancements to be predicted on the basis of material composition, deuteration level, and radical concentration.

Rate-law descriptions have previously been used to describe solid-effect DNP[25,26] and may be similarly justified for the cross-effect.[19,27] Notably, rate-law approximations are consistent with the Genack-Redfield model,[28] which is a magnetic analogue of the Nernst-Planck equation that may partially account for the physical origin of the spin-diffusion barrier. While spin-diffusion in

a homogeneous magnetic field is non-activated, the presence of a strong local magnetic field gradient imposes an energy barrier impeding polarization transfer. We show how under conditions of both microwave irradiation and MAS, simple analytical solutions to the Genack-Redfield model may be obtained by dimensional scaling analyses. By analyzing transient polarization levels of a bulk ^{1}H spin ensemble and determining apparent rate coefficients, detailed quantitative insights may be obtained regarding the nature of quantum interfaces (*e.g.*, the spin-diffusion barrier) and other rate-limiting processes that emerge in complex spin systems.

2. Dimensional Scaling Analyses

Polarization transfer from a dilute paramagnetic center

Classical descriptions have long been used to describe certain spin-relaxation phenomena and energy conduction processes in large coupled spin systems.[29] Under the spin-temperature hypothesis,[30] the relationship between Zeeman energy and spin polarization is analogous to the relationship between thermal energy and temperature. The Zeeman energy refers to the potential energy experienced by a spin ensemble in the presence of a magnetic field, which maintains a Boltzmann distribution of spin states yielding net magnetization, the origin of NMR signal intensity. Although transient polarization transfer processes are complicated, it has been shown[24,31] that the net nuclear magnetization oriented with respect to a static magnetic field (B_0) obeys simple nuclear-spin relaxation relations that are amenable to thermodynamic descriptions. In hyperpolarization schemes, electron spin excitation processes are used to transfer excess Zeeman energy to a spin system to generate non-Boltzmann (*i.e.*, hyper) polarization that leads to dramatically improved NMR signal sensitivity. Zeeman energy transfer occurs from regions of high to low polarization via dipole-mediated spin flips[29] in a strongly coupled ensemble, which propagates over length scales that are suitable for a continuum description.[24] The Zeeman heat capacity is given by $C_z = CB_0{}^2$, where C is Curie's constant, and B_0 is the magnetic field strength.[32] Notably, this implies that the Zeeman heat capacity of an ensemble of nuclear spins can vary spatially with respect to the inhomogeneous local field B_{loc} that are induced near a paramagnetic center. For I = ½ nuclei such as ^{1}H under MAS, $C_{z,n} = \gamma_n \hbar B_0 N_A$, where γ_n is the gyromagnetic ratio and N_A is Avogadro's number, C_z = 2.54x10^{-2} J/mol for ^{1}H nuclei at 9.4 T far from the paramagnetic center where magnetic fields are homogeneous. With the spin polarization, $\tilde{P}$, normalized with respect to Boltzmann equilibrium, the Zeeman energy flux, can be expressed as $q_n = -\rho_n C_{z,n} \mathcal{D}_n \nabla \tilde{P}$, where ρ_n is the spin density (mol·m^{-3}) and $\mathcal{D}_n$ is the spin diffusion coefficient (m^2·s^{-1}). In the rigid limit,[33] spin diffusivities scale as $\mathcal{D}_n \propto \gamma_n{}^2 \rho_n{}^{1/3}$ and can be directly measured[34–36] or predicted under MAS conditions by reduced Liouville space calculations.[37] A transient energy balance for the equilibration of polarization, $\tilde{P}(t)$ among ^{1}H nuclei in a diamagnetic spin ensemble (*e.g.*, the frozen DNP-solvent) yields:

$$\rho_H C_z \frac{\partial \tilde{P}}{\partial t} - \nabla \cdot (\rho_H C_z \mathcal{D}_H \nabla \tilde{P}) = \rho_H C_z \frac{(1-\tilde{P})}{T_1} + \dot{Q}\,, \tag{1}$$

where $\dot{Q}$ (W/m^3) is the DNP source term associated with the microwave excitation and hyperfine processes that generate hyperpolarization. In a bulk solid, such hyperpolarization propagates by spin diffusion and dissipates at a rate of $T_1{}^{-1}$, the inverse of the ^{1}H spin-lattice relaxation time (measured as described in the Supplementary Information, Section S1). This constitutive model is valid for coupled nuclear spin ensembles in homogeneous fields and for polarization transfer across interfaces.

However, because hyperpolarization emanates from paramagnetic centers where local fields (B_{loc}) are inhomogeneous (Fig. 1a), thermodynamic models such as Eq. 1 implicitly rely on knowledge of electron-nuclear interactions that are not easily measured directly.[15] By analogy to Newton's law of cooling, this can be circumvented by use of a DNP polarization-transfer coefficient (k_{DNP}, with units of m/s), where the Zeeman energy flux, $q_H = -(\rho_H C_z k_{DNP}) \Delta\tilde{P}$, is defined at the spin-diffusion barrier interface r=λ_{sdb}. The grouping, $\rho_H C_z k_{DNP}$, has units of W/m^2 per polarization-level and is mathematically analogous to a heat-transfer coefficient (W/m^2·K), but here represents polarization transfer across a thin local magnetic field gradient. Far from paramagnetic centers ($r \geq \lambda_{sdb}$), the DNP generation rates, $\dot{Q}$, are negligible. Assuming that polarization propagates radially (via dipolar couplings) from each paramagnetic center, the Zeeman energy flux into the bulk ensemble can be represented by a Neumann boundary condition:

$$\rho_H C_z \mathcal{D}_H \frac{\partial \tilde{P}}{\partial r}|_{\lambda_{sdb}} = (\rho_H C_z k_{DNP}) \Delta\tilde{P}\,, \tag{2}$$

where $\Delta\tilde{P} \equiv (\overline{P}_{CE} - \tilde{P}|_{\lambda_{sdb}})$ is the polarization difference between $\overline{P}_{CE}$, the effective polarization generated among hyperfine-coupled core nuclei by cross-effect exchange or other DNP mechanisms,[12] and $\tilde{P}|_{\lambda_{sdb}}$, the polarization at the thermal contact interface between core and bulk nuclei given by, λ_{sdb}, the barrier radius. In the context of the Genack-Redfield model, the barrier radius λ_{sdb} corresponds to a 'vortex radius' over which spin diffusion is partially suppressed due to the influence of the strong local inhomogeneous field B_{loc}. This imposes an energy barrier that can result in a steep reduction in steady-state hyperpolarization levels near the paramagnetic centers as recently corroborated by quantum mechanical simulations.[18] Thus, λ_{sdb} has a physical significance that is at least partially analogous to the Debye length in electrolyte solutions,[38] which corresponds to

a characteristic length scale over which ion density surrounding a charged interface varies with respect to a decaying local electric field. Whereas the Debye length represents a the distance over which charge neutrality is violated due to electrostatic screening, the spin-diffusion barrier radius may represent a distance over which hyperfine-coupled nuclei undergo frequency-shifted spin precession that can impede or alter spin-diffusion rates.[15,17,18]

Previous experimental and theoretical estimates of the barrier radius λ_{sdb} have ranged from 0.3 to 1.7 nm for monoradical species, due to differences in experimental conditions and differing definitions of the spin-diffusion barrier.[16] Here, we define the spin-diffusion barrier λ_{sdb} as the characteristic scaling distance over which local properties (e.g., spin-diffusion coefficient $\mathcal{D}_{\mathrm{H}}$ and spin-lattice relaxation times) approach bulk values. It is anticipated that λ_{sdb} is related to the pseudopotential radius, derived in the continuum limit by de Gennes[31] and Khutsishvili,[39] which represents a characteristic length scale over which direct paramagnetic relaxation and spin-diffusion compete. A similar theory was advanced by Goldman[40] and an experimental value of 1.7 nm reported for the steep transition in the local diffusion rate, albeit under static, low field, and low temperature conditions. Based on these past studies, λ_{sdb} has a complicated dependence on sample composition, field strength, and MAS rate, and analysis of the spin-diffusion barrier under DNP NMR conditions remains an active area of research.[15,18,24]

Although λ_{sdb} values are not explicitly known, it is nevertheless still possible to estimate the apparent rate of polarization transfer across the barrier by means of a film approximation. For the case of hyperpolarization transfer considered here, the DNP polarization-transfer coefficient k_{DNP} (m/s) is defined in Eq. 2 and notably accounts for the rate of polarization transfer to the bulk spin ensemble; $\overline{P}_{\mathrm{CE}}$ accounts for the polarization gain. For the biradical AMUPol species in glycerol-water, the spin-diffusion barrier is taken to be λ_{sdb} = 1.8 nm from the biradical center, an estimate that is larger than the 1.2 nm electron-electron separation distance of the commonly used AMUPol biradical.[41] For r > 1.8 nm, ^{1}H-^{1}H dipolar coupling strengths and T_1 relaxation times are considered to be negligibly affected by the biradical species and considered to approach bulk values within the diamagnetic matrix. As such, the estimate of λ_{sdb} = 1.8 nm represents an approximate upper-bound on the dimensions of the spin-diffusion barrier that have previously been reported. For the cross-effect mechanism, an upper-theoretical-limit for $\overline{P}_{\mathrm{CE}}$ is γ_e/γ_H=658, although lower values are often encountered, due to electron spin-relaxation effects[42,43] or due to an inhomogeneous distribution of microwave intensity.[44] Typically, film coefficients are measured empirically (e.g., using Eq. 2) and are used to develop relations for different conditions and to provide insights on scaling dependences.[45] By analogy to film theory for mass transfer, assuming steady-state transfer and that spin diffusion is rate-limiting:[1]

$$k_{\mathrm{DNP}} \sim \frac{\mathcal{D}_{\mathrm{H}}}{\Delta\lambda} \quad , \tag{3a}$$

which indicates that the polarization-transfer coefficient (m/s) is expected to scale linearly with the spin-diffusion coefficient (m^2/s) over an indeterminate film thickness $\Delta\lambda$; a similar approach invoking a "heterogeneous reaction velocity" (m/s) was introduced by Nernst.[46] Or by analogy to a related mass transfer model by Danckwerts,[47] for the more general case where the rates of spin diffusion, spin-lattice-relaxation, and polarization generation are comparable:

$$k_{\mathrm{DNP}} \sim \sqrt{\mathcal{D}_{\mathrm{H}}\omega} \quad , \tag{3b}$$

indicating that the polarization transfer coefficient varies as the square root of the product of the diffusion coefficient (m^2/s) and a "surface renewal frequency" ω (s^{-1}). In mass transfer, ω may correspond to the circulation of eddy currents, which periodically replenish the solute concentration at a gas—liquid interface in contact with a bulk liquid. For DNP NMR, cross-effect transfer events may occur at some frequency ω, replenishing hyperpolarization within the barrier that subsequently diffuses into the bulk. Although, Eqs. 3a,b do not account for T_1 relaxation, both mass transfer models have been solved for the mathematically analogous condition of a first-order irreversible chemical reaction.[48] Given the success of *ab initio* simulations in modelling cross-effect DNP,[18,23] it is anticipated that quantum mechanical calculations will afford more detailed local mechanistic insights than can be obtained by a film theory. However, the latter provides complementary quantitative information on hyperpolarization transfer through heterogeneous solid media over much larger length scales (> 1.8 nm), as has similarly been applied to the design and optimization of industrial process equipment.[1,45] The polarization-transfer coefficient k_{DNP} thus provides a means to quantify rate limitations, predict sensitivity improvements, and establish scaling dependences in a simple experimental formulism. For example, it is generally known how a heat transfer coefficient scales with fluid velocity, and it would be similarly useful to know how a polarization-transfer coefficient scales with ^{1}H spin density, field strength, or MAS rate under DNP-NMR conditions. As will be presented and discussed below, k_{DNP} and $\overline{P}_{\mathrm{CE}}$ together provide a foundational basis for a continuum description of large composite spin systems when used in combination with dimensional analyses.

The relative rates of generation, propagation, and dissipation of hyperpolarization can be compared by using a scaling analysis, which leads to dimensionless parameters that are analogous to those characteristic of classical energy or mass transfer processes. Specifically, nondimensionalizing Eq. 1 for $\tilde{r} = r/L$ and $\tilde{t} = t/T_1$ yields:

$$\frac{\partial \tilde{P}}{\partial \tilde{t}} - \phi_P^{-2}\left(\frac{2\partial \tilde{P}}{\tilde{r}\partial \tilde{r}} + \frac{\partial^2 \tilde{P}}{\partial \tilde{r}^2}\right) = (1-\tilde{P}) \,, \tag{4}$$

where the dimensionless parameter $\phi_P \equiv L/(\mathcal{D}_H T_1)^{0.5}$ arises naturally along with a characteristic dimension $L=(\lambda_{ws}^3-\lambda_{sdb}^3)/3\lambda_{sdb}^2$, which corresponds to a classical spin packet around each paramagnetic center to which energy is transferred. The spin packet is defined by a Wigner-Seitz sphere (Fig. 1b), which is an imaginary spherical volume around a single biradical molecule that is equivalent to the bulk volume density of biradical species in the DNP matrix. Importantly, the Wigner-Seitz radius, λ_{ws}, becomes progressively larger at lower biradical concentrations,[24] corresponding for example to values of 5.8 nm and 3.2 nm at 2 mM or 12 mM biradical (here, AMUPol in glycerol-water), respectively. At the center of this sphere, there is an ensemble of core nuclei within the radius of the spin-diffusion barrier, λ_{sdb}, that are in poor thermal (i.e., polarization) contact with the bulk. By convention, In similar heat transfer analyses, L typically is taken to be the ratio of the volume and thermal contact area, as given above. The parameter ϕ_P is analogous to the well-known Thiele modulus associated with mass transfer in heterogeneous catalysts, but, in the present context, ϕ_P represents the relative rates of polarization transfer by spin diffusion and energy dissipation by spin-lattice relaxation.

Similarly, nondimensionalization of the boundary condition in Eq. 2 yields $\partial\tilde{P}/\partial\tilde{r} = Bi_P\Delta\tilde{P}$, where $Bi_P \equiv k_{DNP}L/\mathcal{D}_H$ corresponds to a dimensionless Biot number. In transient heat transfer processes, the Biot number reflects the rate of heat transfer at the surface of an object relative to the rate of internal heat conduction within its body.[49] Low Biot number conditions indicate that a solid medium is "thermally thin" on the basis of its internal transport properties, its dimensions, and the rate at which energy is delivered to or dissipated from it, as shown schematically in Fig. 2a. For a thin cooling fin, internal temperature gradients can be neglected, thereby enabling simple analytical descriptions of transient heat exchange, *e.g.,* by means of a lumped-element approximation.[49] This has direct analogy to polarization transfer processes, where the Biot number reflects the rate of polarization transfer across the spin-diffusion barrier relative to the rate of spin diffusion within a diamagnetic bulk solid. For spherical geometries with Bi_P <0.65 (derivation in S.I., Sections S2, S3), spin-diffusion resistances can be considered negligible, and hyperpolarization will be distributed essentially instantaneously and uniformly ($\nabla^2\tilde{P}=0$) into the bulk spin ensemble over a characteristic time scale (*e.g.*, T_{DNP}), as depicted in the upper solid trace of Fig. 2b. For DNP NMR, the condition "thermally thin" (low Biot number) indicates that polarization transfer across the spin-diffusion barrier is rate-limiting, and that build-up times in the surrounding matrix do not depend significantly on bulk spin-diffusion properties.

Furthermore, small values of Bi_P justify the use of a lumped-element approximation, similar to those employed in transient heat transfer analyses. For such an approximation (Bi_P<0.65), the rate of spin diffusion within a bulk diamagnetic matrix can be considered infinitely fast relative to the rate of exchange across the spin diffusion barrier, the latter of which as a consequence will be rate-limiting. This allows the boundary condition (Eq. 2) to be transformed into a uniform source term, $\dot{Q} = \rho_H C_z k_{DNP} L^{-1} \Delta \tilde{P}$, as detailed in Section S2 of the S.I. The consequence of this is that the DNP matrix can be regarded as a homogeneous continuum, rather than as ~10^{16} interacting spin packets. In this description, the continuum element is the spin packet defined by the Wigner-Seitz sphere. For an initial condition $\tilde{P}(r,0) = 0$ corresponding to saturation recovery, an analytical expression is obtained for the characteristic time to build-up polarization, T_{DNP}^o:

$$T_{DNP}^o = \frac{T_1^o}{(1 + k_{DNP}L^{-1}T_1^o)} \,, \tag{5a}$$

$$k_{DNP}L^{-1} = \frac{T_1^o - T_{DNP}^o}{T_1^o T_{DNP}^o} \,, \tag{5b}$$

from which k_{DNP} is straightforwardly obtained from experimentally measured values of T_1^o and T_{DNP}^o, and known values of L ; the superscript 'o' denotes properties of spin packets isolated from dipolar contact with dissimilar spin reservoirs. Here, the characteristic build-up time, T_{DNP}^o, is associated with cumulative polarization transfer between core and bulk nuclei in a homogeneous frozen matrix and the spin-lattice relaxation time, T_1^o, is that of the bulk nuclei in the absence of biradical species. Eq. 5b manifests the direct relationship between $k_{DNP}L^{-1}$ and experimental values for T_1^o and T_{DNP}^o, which are conveniently measured even if the spin-diffusion barrier radius is not explicitly known. Importantly, under low Biot conditions, the film transfer model accounts for the mono-exponential kinetics for polarization build-up that are commonly observed for ^{1}H spin-diffusion-mediated DNP-NMR experiments in frozen biradical matrices.[24,26,27] From measured build-up times, values for k_{DNP} are determined using Equation 5a and yield quantitative insights into rate-limiting polarization transfer processes. Specifically, k_{DNP} is an apparent rate constant which lumps together the contributions of hyperfine interactions, relaxation processes, and slow diffusion steps that limit apparent polarization transfer rates between core and bulk nuclei.

As demonstrated in Eq. 5a, for a similar transfer coefficient, k_{DNP}, and a similar biradical concentration, by means of L, it is expected that shorter bulk T_1^o values will directly correspond to shorter characteristic build-up times (T_{DNP}^o). This phenomenon can be understood by analogy to the mass transfer enhancement factor (E) which for spin polarization is:

$$E \equiv \frac{\text{polarization transfer rate (with relaxation)}}{\text{polarization transfer rate (no relaxation)}} \quad ,$$

the ratio between the polarization transfer rate in the presence of T_1^0 relaxation versus the polarization transfer rate in the absence of T_1^0 relaxation. Thus, the depletion of polarization increases the $\nabla\tilde{P}$ driving force resulting in a greater polarization transfer rate within the barrier. Numerical simulations for the E factor have been tabulated by van Krevelen and Hoftijzer,[50] and are reported on a non-dimensional basis with respect to the Hatta number (Ha). The spin polarization analogue of the Hatta number is Ha = $(\mathcal{D}_H T_1^{-1})^{0.5}/k_{DNP}$, and provides the ratio between the rate of relaxation *within the barrier region* versus the apparent polarization transfer rate *into the barrier region*. For larger Ha number, polarization levels are expected to be depleted across the barrier from that of core nuclei, $\overline{P}_{CE}$, to that of bulk nuclei, $\tilde{P}|_{\lambda_{sdb}}$, consistent with recent *ab initio* simulations.[18] To avoid referring to the quantity, *E*, as a polarization transfer rate enhancement, hyperpolarization transfer away from paramagnetic centers accelerated by nuclear relaxation will be hereafter described as a "spin Hatta effect". Such effects influence polarization build-up times and absolute polarization gains in DNP NMR experiments.

Although cross-effect DNP is routinely used to enhance NMR signal intensity, determining absolute polarization levels is challenging,[51–53] even for low Bi_P conditions for which the polarization level of the diamagnetic bulk is nearly uniform. The effective polarization levels generated by cross-effect transfer can be obtained by lumped-element solution of Eq. 1 under conditions with and without microwave irradiation, $\overline{P}_{CE(on)}$ and $\overline{P}_{CE(off)}$ respectively, which yield:

$$\varepsilon_\theta^0 = \frac{1 + k_{DNP} L^{-1} \overline{P}_{CE(on)} T_1^0}{1 + k_{DNP} L^{-1} T_1^0} \quad , \qquad (6)$$

$$\theta_{depo}^0 = \frac{1 + k_{DNP} L^{-1} \overline{P}_{CE(off)} T_1^0}{1 + k_{DNP} L^{-1} T_1^0} \quad , \qquad (7)$$

where ε_θ^0 and θ_{depo}^0 are the mean steady-state polarization levels[54] in the bulk with or without microwave irradiation respectively, normalized with respect to thermal equilibrium. For dilute paramagnetic centers, ρ_{pc}, these quantities are directly related to the commonly reported signal enhancement, $\varepsilon_\infty^0 \approx \varepsilon_\theta^0/\theta_{depo}^0$, which is the ratio of NMR signal intensity with and without microwave irradiation, as discussed in the Methods section below. Here, $\overline{P}_{CE(on)}$ provides an upper-bound for polarization levels that are attainable among bulk ^{1}H nuclei under microwave irradiation, and $\overline{P}_{CE(off)}$ quantifies the extent of MAS-induced depolarization, which in the absence of microwave irradiation, results in partial inversion of the nuclear spin ensemble to polarization levels below thermal equilibrium,[53,54] as depicted schematically in the lower traces of Fig. 2. For dilute paramagnetic centers, low Bi_P conditions prevail for strongly coupled nuclei (*e.g.*, ^{1}H, ^{19}F, ^{31}P), while high Bi_P conditions are expected for dilute or low-γ nuclei (*e.g.*, ^{13}C, ^{15}N, ^{29}Si) which have weaker dipole interactions. Furthermore, the relationships developed in Eqs. 5a, 6, and 7 provide the means to estimate polarization build-up times and signal gain for materials with different compositions and bulk spin-lattice relaxation properties. These expressions yield quantitative results that are in close agreement with recent quantum mechanical simulations[23] (see Supporting Information, Section S6, Fig. S5) that describe relationships between T_1, T_{DNP}, and ε_θ^0, which validate the film-theory approach and scaling analyses presented here. The analyses indicate that the evolution of a system towards steady-state, e.g., as reflected by the polarization build-up time (Eq. 5a), can be inferred from steady-state polarization gains (Eqs. 6 and 7). This suggests that time-saving *ab initio* simulations[18,22] used to calculate steady-state polarization profiles may also be useful for predicting polarization build-up times and in identifying rate-limiting polarization transfer processes.

3. Results/Discussion

Hyperpolarization transfer rates

Whereas hyperpolarization transfer by the cross-effect[19] occurs on the order of microseconds to milliseconds and ^{1}H spin diffusion between paramagnetic centers occurs on the order of tens of milliseconds,[24] the characteristic time (T_{DNP}^0) is often several seconds, indicating the presence of a slow-exchange step.[26] Were this slow-exchange step overcome, many applications which rely on the detection of insensitive spin pairs could be greatly expedited.[55] For DNP-NMR experiments involving water-soluble biomolecules at conventional 9.4 T field strengths, the benchmark DNP matrix consists of frozen glycerol-water 60/30/10 (d_8-glycerol/D_2O/H_2O) solutions containing AMUPol, a stable nitroxide biradical.[56] Although this system has been empirically optimized, the accumulation of non-Boltzmann polarization levels depends on the competitive rates of spin polarization generation, spin diffusion, and spin relaxation which have not been systematically elucidated. As shown in Fig. 3a, measured values of the characteristic times T_1^0 and T_{DNP}^0 are strongly influenced by the volumetric ^{1}H spin density (ρ_H) which can be adjusted from 0 to 110 M for glycerol-water systems. The ^{1}H spin-lattice relaxation time (T_1^0) is strongly dependent on ^{1}H-^{1}H dipole-dipole couplings and varies by an order of magnitude from 20 – 200 s over the measured ρ_H range. In the presence of AMUPol, characteristic build-up times (T_{DNP}^0) are correspondingly shorter due to electron-nuclear interactions which propagate through the lattice.

Although T^{o}_{DNP} values are often considered a metric of DNP performance, they inherently depend (Eq. 5a) on properties of the matrix and are shorter at higher biradical concentrations.[57,58] The polarization transfer coefficient, k_{DNP}, depends on the effective local environment near the paramagnetic centers ($r < \lambda_{sdb}$), as opposed to the extensive properties of the bulk nuclear spin ensemble to which they are coupled. In Fig. 3b, k_{DNP} values are plotted versus the cube root of the ^{1}H density $\rho_H^{1/3}$ of the frozen DNP matrix, which scales proportionally with the mean ^{1}H–^{1}H distance and the ^{1}H spin-diffusion coefficient $\mathcal{D}_H$ in a homogeneous magnetic field, as discussed above. Importantly, for all conditions measured in Fig. 3, Bi_P <<0.65, which corresponds to polarization transfer between core and bulk nuclei being rate-limiting and which also validates the use of the lumped-element approximation. Because spin flips rely on dipolar couplings, the effective rate of polarization transfer across the spin-diffusion barrier, as reflected by k_{DNP}, is expected to be sensitive to matrix ^{1}H spin density. For the specific case where ρ_H = 20 M, $\mathcal{D}_H$ is estimated to be ~330 nm^2/s, as scaled $(\mathcal{D}_H \sim \rho_H^{1/3})$ from a measured value of 5.8 x 10^{-16} m^{-2}s^{-1} for polystyrene (ρ_H = 70 M) under similar DNP-enhanced MAS NMR conditions.[36] For typical DNP-NMR analyses (e.g., 1–16 mM AMUPol in glycerol-water matrices at 100 K, 9.4 T, and 12.5 kHz MAS), low Biot numbers will generally result for biradical concentrations >0.25 mM, as depicted in Fig. 2a. Consequently, under such conditions, ^{1}H polarization build-up times will not depend on bulk ^{1}H spin-diffusion rates and are expected to exhibit mono-exponential behavior (see Supporting Information, Section S1, Fig. S2). Larger k_{DNP} values correspond to more effective polarization transfer across the barrier region and generally manifest shorter T_{DNP} buildup times, as observed here.

Interestingly, two regimes are observed in Fig. 3b with distinct linear dependences of k_{DNP} on $\rho_H^{1/3}$ associated with different rate-limiting polarization-transfer processes. The positively sloped linear-dependence of k_{DNP} on $\rho_H^{1/3}$ matches the predicted scaling relationship in Eq. 3a, which describes relatively slow diffusion across a barrier. For low ^{1}H spin densities (ρ_H<17 M), k_{DNP} values tend to be small as a consequence of weak ^{1}H–^{1}H dipolar couplings, so that it is speculated that spin diffusion limits the rate at which hyperpolarization is propagated to the bulk. Generally, for higher ρ_H, ^{1}H dipolar couplings become stronger, resulting in more effective polarization transfer, as manifested by larger values for k_{DNP}, though only up to a point. At high ρ_H values, there are more ^{1}H nuclei to polarize per biradical and shorter ^{1}H T_1 relaxation times, which render the DNP matrix and barrier region a stronger polarization sink. A subtle inversion point between regimes is identified by determination of $k_{DNP,}$ which by Eq. 5a, is intrinsically related to known or measured values of T_1^o, T^o_{DNP}, and AMUPol concentration (ρ_{pc}), the latter by means of, L, the characteristic spin packet length. The maximum value of k_{DNP} occurs for ρ_H =17 M ($\rho_H^{1/3}$=2.55 M$^{1/3}$), above which k_{DNP} values decrease with increasing ^{1}H spin density. This spin-exchange-limited regime is representative of the complicated dissipative spin dynamics occurring near paramagnetic centers, which depend upon the relative rates of cross-effect DNP, ^{1}H spin-lattice relaxation, ^{1}H spin-spin relaxation, or cross-relaxation phenomena.[16,17] This is consistent with similar kinetic phenomena reported for solid-effect DNP, where build-up times for polarization agents such as Gd-DOTA are highly sensitive to ^{1}H spin density and plateau at ~20 M, compared to trityl radicals that are less sensitive to such effects.[26] Together, prior literature[15,18,20,24] and the present analyses indicate that the influence of the spin-diffusion barrier can greatly depend on the structure of the polarizing agent.

Here, polarization transfer kinetics are phenomenologically encompassed within the polarization transfer coefficient, k_{DNP}, the proportionality constant associated with the apparent rate of transfer across the spin-diffusion barrier, which can be used to predict polarization build-up times under different experimental conditions. As defined in Eq. 2, the product, $\rho_H C_z k_{DNP}(\overline{P}_{CE} - \tilde{P}(t))$ corresponds to the Zeeman energy flux entering the bulk DNP matrix at λ_{sdb} = 1.8 nm, the barrier radius in the film approximation. Larger k_{DNP} values correspond to larger hyperpolarization transfer rates relative to the ^{1}H spin density (an intensive property of the matrix) and more effective transfer between core and bulk nuclei. As indicated in Eq. 5a, measuring the bulk solvent T_1^o relaxation time permits k_{DNP} to be determined. The data in Fig. 3a,b correspond to polarization build-up times $T^o_{DNP(on)}$ in the presence of microwave irradiation, which are slightly different than those measured in the absence of microwaves $T^o_{DNP(off)}$ (see Supporting Information Section S1, Table S1 and Fig. S2). The normalized transient signal enhancement factor, $\varepsilon(t)$, can be defined as:

$$\varepsilon(t) = \frac{1 - \exp\left(-\frac{t}{T^o_{DNP(on)}}\right)}{1 - \exp\left(-\frac{t}{T^o_{DNP(off)}}\right)}, \qquad (8)$$

which can be plotted as a function of the recycle delay time to also distinguish the kinetic regimes associated with the different rate-limiting polarization transfer processes, even without explicit knowledge of T_1^o values. Figure 4a,b shows plots of the enhancement factor $\varepsilon(t)$, as functions of the recycle delay time for different concentrations (2 mM and 12 mM) of the AMUPol biradical species in glycerol-water matrices with different ^{1}H densities. Interestingly, for short recycle delays, the plots exhibit values of $\varepsilon(t)$ < 1 at low ^{1}H spin densities and $\varepsilon(t)$ > 1 at high ^{1}H spin densities, with the crossover points occurring at ~13 M for both 2 and 12 mM AMUPol, similar to the optimum value of the DNP transfer coefficient at ca. 17 M in Fig. 3b. The behavior observed for $\varepsilon(t)$ < 1 is consistent with slow and steady transfer of hyperpolarization to the bulk, consistent with slow spin diffusion, as depicted in Fig. 4c. For these conditions, $T^o_{DNP(off)}$ will be slightly shorter than $T^o_{DNP(on)}$, due to classical spin thermodynamic considerations;[24] the initial state is closer to the final state in the absence of microwaves. The significance of

$\varepsilon(t)$> 1 is that paramagnetic relaxation effects dominate the polarization transfer kinetics across the barrier (Fig. 4d), as has been previously observed for heterogeneous matrix-particle suspensions with dissimilar relaxation times.[36,59,60] Together, the results in Fig. 3b and Fig. 4a,b suggest that net hyperpolarization transfer rates into the bulk are optimized near the point of crossover between the two regimes. For both limiting cases, mono-exponential build-up occurs among bulk nuclei $\tilde{P}(t)$ because polarization is rapidly and uniformly distributed over $\lambda_{sdb} < r < \lambda_{WS}$ at low Biot number conditions (Bi_P<0.65). These analyses corroborate that the "spin-diffusion limited" regime is characteristic of slow spin diffusion, and that the "spin-exchange limited" regime is characteristic of fast spin-lattice relaxation within the barrier region. Interestingly, the $\rho_H^{1/3}$-dependence of the transfer coefficient resembles a Sabatier diagram,[61] which in heterogeneous catalysis, relates the adsorption enthalpy of a reactant to its apparent reaction rate; reaction rates are likewise highest for species with intermediate adsorption enthalpies. Here, polarization-transfer kinetics across an inhomogeneous field gradient are most effective at an intermediate value of ρ_H for which ^{1}H–^{1}H dipole-dipole interactions are sufficient to relay polarization without contributing excessively to dissipative spin dynamics (*e.g*, spin-lattice relaxation). These insights are consistent with quantum mechanical treatments that have attributed solid-effect DNP in large systems to a "kinetically constrained diffusion" mechanism.[13]

Hyperpolarization levels generated by cross-effect DNP

Even if hyperpolarization transfer rates are slow, it is possible to accumulate large amounts of hyperpolarization, provided spin-lattice relaxation times are long. Understanding the extent of signal sensitivity enhancement achieved by DNP-NMR, however, can be challenging. As discussed above for absolute ^{1}H polarization levels,[51,53,54] the situation is simplified when the paramagnetic centers are dilute (*e.g.*, ρ_{pc}=2 mM), so that paramagnetic quenching is negligible.[57,58] Due to strong hyperfine interactions, ^{1}H spins in closest proximity to paramagnetic centers ($r << \lambda_{sdb}$) are typically quenched or rendered otherwise NMR "invisible". Nevertheless, these hyperfine-coupled ^{1}H spins are directly polarized by cross-effect transfer, and the resulting hyperpolarization is propagated by spin diffusion to more distant ^{1}H spins in the diamagnetic bulk ($r > \lambda_{sdb}$). Importantly, $\overline{P}_{CE}$ is indicative of the efficacy of cross-effect transfer for a given set of experimental conditions and corresponds to the magnitude of the effective hyperpolarization that is transferrable directly to hyperfine-coupled ^{1}H nuclei and indirectly to more distant ^{1}H nuclei.

For cross-effect DNP, quantum conversion depends on the effective polarization difference between two coupled electron spins (*i.e.*, a nitroxide biradical) which satisfy a cross-effect frequency matching condition.[12,20,27] Partial saturation by microwave irradiation maintains an effective polarization difference between electron spins driving hyperpolarization transfer; however, in the absence of microwave irradiation, the cross-effect matching condition may still be satisfied under magic-angle-spinning, leading to depolarization effects.[19,62] Fitting the measured enhancements ε_∞^0 and θ_{depo}^0 in Fig. 5 using Eqs. 6 and 7 and ρ_H-dependent values for T_1^0 and k_{DNP} (Fig. 3a,b) yields the blue and grey solid lines, which interestingly correspond to constant values for $\overline{P}_{CE(on)}$=148±14 and $\overline{P}_{CE(off)}$=0.42±0.09. The close agreements of the model fits with measured ε_∞^0 and θ_{depo}^0 values establish that $\overline{P}_{CE(on)}$ and $\overline{P}_{CE(off)}$ are, under the conditions used, independent of the ^{1}H spin density in the frozen matrix (within experimental uncertainties) for 2 mM AMUPol. This suggests that a fixed polarization level is induced among hyperfine-coupled ^{1}H nuclei, even as the number of electron-nuclear spin pairs is increased; in other words, the electron spin reservoir is not depleted appreciably by hyperfine transfer to nuclear spins. For constant $\overline{P}_{CE(on)}$, the biradical maintains the capacity to polarize nearby ^{1}H nuclei, although enhancement values decline at higher ^{1}H spin densities, due to a decreasing rate of polarization transfer, k_{DNP}, and shorter bulk T_1 values. (It is unclear whether this observation would hold if the biradical molecule itself were deuterated, because ^{1}H-containing moieties of the biradical may participate in spin-diffusion.[15,18,63]) To our knowledge, the dependence of $\overline{P}_{CE}$ on AMUPol concentration has not been established, although it is anticipated that $\overline{P}_{CE}$ will be influenced by biradical concentrations that will effect inter-radical separation distances. Strong electron-electron dipole interactions,[19,58] which can be expected at higher AMUPol concentrations or from radical clustering,[27] may decrease $\overline{P}_{CE(on)}$ values, due to enhanced electron spin-relaxation effects that diminish the efficacy of cross-effect DNP. For a similar $\overline{P}_{CE}$ driving force, longer bulk T_1^0 values result in greater accumulation of hyperpolarization (larger ε_θ^0, Fig. 5). From previous *ab initio* simulations,[23] it has been shown that $\overline{P}_{CE}$ values can be extracted from a plot of T_1 vs. ε_θ^0 by taking the limit as the bulk T_1 value approaches infinity (see SI, Section S6). DNP injection rates in units of Watts are calculated for 2 mM AMUPol in glycerol-water in SI Section S7. The analytical expressions obtained from the lumped-element analysis thus relate the rate of Zeeman energy generated by an ensemble of biradicals ($\dot{Q}$) to the macroscopically observable accumulation of ^{1}H spin hyperpolarization in a surrounding diamagnetic spin bath (*e.g.*, the frozen matrix).

Hyperpolarization of solid-particle targets

An advantage of DNP-NMR is that hyperpolarization emanates from paramagnetic centers, enabling surface-enhanced NMR spectroscopy of porous or nonporous solids. As shown schematically in Fig. 1, hyperpolarization is transferred across the spin-diffusion barrier and is relayed by ^{1}H spin diffusion into the solid-particle interior up to µm length scales. With ρ_H, ρ_{pc}, T_1, k_{DNP}, and $\overline{P}_{CE}$ known, polarization transfer kinetics can be predicted, including across interfaces in heterogeneous systems. For polarization transfer to a solid particle (*S*) in dipole-dipole contact with a DNP matrix (*M*), the process is analogous to energy conduction through a series of thermal resistances and can be treated similarly for each region *i*, such that:

$$\rho_{\mathrm{H},i}C_{\mathrm{z}}\frac{\partial\tilde{P}_i}{\partial t}-\nabla\cdot\left(\rho_{\mathrm{H},i}C_{\mathrm{z}}\mathcal{D}_{\mathrm{H},i}\nabla\tilde{P}_i\right)=\rho_{\mathrm{H},i}C_{\mathrm{z}}\frac{\left(\Pi_i-\tilde{P}_i\right)}{T^{\mathrm{o}}_{\mathrm{DNP},i}}, \quad (9)$$

where Π_i is equal to either $\varepsilon^{\mathrm{o}}_{\theta,\mathrm{i}}$ or $\theta^{\mathrm{o}}_{\mathrm{depo},i}$ in the presence or absence of microwave irradiation as determined from Eqs. 6-7. Similarly, the characteristic time, $T^{\mathrm{o}}_{\mathrm{DNP},i}$, is determined from Eq. 5a by using known or measured values of $T^{\mathrm{o}}_{1,i}$, $k_{\mathrm{DNP},i}$, and L_i, as described above. For example, 2 mM AMUPol in glycerol-water ($\rho_{\mathrm{H,M}}$=12 M) yields values of $\varepsilon^{\mathrm{o}}_{\theta,M}$=120, $\theta^{\mathrm{o}}_{\mathrm{depo},M}$=0.53, and $T^{\mathrm{o}}_{\mathrm{DNP},M}$=16 s for the conditions in Figs. 3 and 5. In contrast, the interiors of solid polystyrene particles without paramagnetic centers ($L_S\rightarrow\infty$) are hyperpolarized solely by ^{1}H spin diffusion, though recover polarization thermally, for which Eqs. 5-7 yield $\varepsilon^{\mathrm{o}}_{\theta,S}$=$\theta^{\mathrm{o}}_{\mathrm{depo},S}$=1 and $T^{\mathrm{o}}_{\mathrm{DNP},S}$ =$T^{\mathrm{o}}_{1,S}$=1.3 s, the latter being the ^{1}H spin-lattice relaxation time of polystyrene at 100 K, 9.4 T, and 12.5 kHz MAS. The interfacial boundary conditions[64] are analogous to those in heat conduction processes, such that the polarization and Zeeman energy flux are continuous across each interface, where $\tilde{P}_i=\tilde{P}_j$ and $q_{\mathrm{H}}|_i=q_{\mathrm{H}}|_j$, respectively. The relative propensity of each region to conduct spin polarization is scaled by the quantity $\rho_{\mathrm{H}}C_{\mathrm{z}}\mathcal{D}_{\mathrm{H}}$, which is the Zeeman conductivity. For polarization transfer between materials with different ^{1}H spin densities, the effects associated with their different Zeeman heat capacities must be taken into account. Deuteration of the frozen solvent matrix tends to increase ^{1}H T_1 relaxation times, which allows for greater accumulation of hyperpolarization, although it also reduces the capacity of the solvent to relay Zeeman energy (by means of $\rho_{\mathrm{H}}C_{\mathrm{z}}\mathcal{D}_{\mathrm{H}}$). In general, partially deuterated frozen glycerol-water matrices propagate Zeeman energy less effectively than ^{1}H-abundant polymeric solids, but, retain hyperpolarization to a greater extent.

In the presence of a solid-particle target, hyperpolarization generated in a DNP matrix must be distributed over relatively large distances (typically 1–100 nm) to reach the particle surface. The extent to which the hyperpolarization is transferred to and propagates into the solid particle depends on the rates of spin diffusion and spin-lattice relaxation in the solid. Assuming hyperpolarization is transferred to the solid particle solely by matrix-mediated spin-diffusion, the polarizability of a spherical sink of radius R is characterized by the Thiele modulus in the solid-particle, $\phi_S\equiv R/(\mathcal{D}_{\mathrm{H},S}T^{\mathrm{o}}_{1,S})^{0.5}$ and effectiveness factor η=$3\phi_S^{-2}(\phi_S\cdot\coth[\phi_S]-1)$, as derived in Section S4 of the S.I. Quantitatively, η represents the ratio of the average rate of Zeeman energy dissipation in the particle interior, compared to the maximum rate that would occur if the particle interior were uniformly polarized to the level at the particle surface yielding an extent of hyperpolarization throughout the object. Larger ϕ_S values correspond to stronger polarization sinks, such that the effectiveness factor is $\eta\rightarrow$ 100 % and $\eta\rightarrow$ 0 % in the limits of $\phi_S\rightarrow 0$ and $\phi_S\rightarrow\infty$, respectively. Importantly, the surface polarization must be maintained by Zeeman energy generation and propagation within the DNP matrix. This requires that the rate of Zeeman energy dissipation within the solid-particle interior be equal to the rate of Zeeman energy flowing into the surface at steady-state satisfying the condition,

$$(q_H\cdot A)|_R=\iiint\rho_{\mathrm{H,S}}C_{\mathrm{z}}\frac{\left(\tilde{P}_S(r)-1\right)}{T^{\mathrm{o}}_{1,S}}\mathrm{d}V \quad , \quad (10)$$

$$\frac{\partial\tilde{P}}{\partial\tilde{r}}|_{\tilde{r}\,=\,1}=\frac{1}{3}\mathrm{Da_P}\eta\left(\tilde{P}|_{\tilde{r}\,=\,1}-1\right) \quad , \quad (11)$$

where Eq. 11 is obtained by nondimensionalizing Eq. 10 with respect to $\tilde{r}$ =r/R and $\tilde{t}$ =$t/T^{\mathrm{o}}_{1,S}$, as detailed in the steady-state analytical solution to Eq. 9 in Section S5 of the S.I. Here, a polarization analogue of the dimensionless Damköhler number ($\mathrm{Da_P}$) is expressed in terms of measurable or known quantities,

$$\mathrm{Da_P}=\frac{R^2{T^{\mathrm{o}}_{1,S}}^{-1}}{\mathcal{D}_{\mathrm{H},M}}\cdot\frac{\rho_{\mathrm{H},S}C_{\mathrm{z}}}{\rho_{\mathrm{H},M}C_{\mathrm{z}}}, \quad (12)$$

for a given ^{1}H spin density of the DNP matrix ($\rho_{\mathrm{H},M}$), the spin-diffusion coefficient of the DNP matrix ($\mathcal{D}_{\mathrm{H},M}$), the ^{1}H spin density of the solid-particle interior ($\rho_{\mathrm{H},S}$), and the ^{1}H spin-lattice relaxation time ($T^{\mathrm{o}}_{1,S}$) in the solid-particle interior. Here, $\mathrm{Da_P}$ may be regarded as a relative measure of the spin-polarization inertia and relates the rate of energy dissipation in the interior versus the rate of DNP matrix-mediated spin-diffusion to the surface, weighted by the specific Zeeman heat capacity of each medium. Spin-polarization inertia is similar to thermal inertia, however while thermal energy (as measured by temperature) can be dissipated, there is no equivalent relaxation-related loss mechanism under these conditions and therefore, a thermal analogue of the Damköhler number does not strictly exist. In a composite heterogeneous spin system, high levels of hyperpolarization at particle surfaces can only be maintained if the polarization inertia of the DNP matrix is sufficient to overcome energy dissipation within the particle interior. Thus, in addition to the kinetic limitations presented by the spin-diffusion barrier, which are encompassed within the DNP source term, $\dot{Q}$, ^{1}H spin thermodynamic properties associated with the DNP matrix (an energy 'source') and the solid-particle target (an energy 'sink') govern polarization transfer in composite systems.

An advantage of dimensionless parameterization is that rate-limiting polarization transfer phenomena can be assessed without computational methods. In Figure 6a-c, the normalized steady-state polarization gain under microwave irradiation, $\varepsilon_{\theta,i}(\tilde{r})/\varepsilon^{\mathrm{o}}_{\theta,M}$, is plotted as a function of the position variable $\tilde{r}$ for different values of the Thiele modulus (ϕ_S) and Damköhler number ($\mathrm{Da_P}$). The plots in Fig. 6a,b are generated using $\mathrm{Da_P}$ = 0.2 and with ϕ_S values of 2.0 and 20, respectively. As a general rule, for

small Damköhler numbers (Da_P<<1), the frozen DNP solvent matrix will resist changes in its polarization level, maintaining a high enhancement at particle surfaces. By analogy to diffusion-reaction processes in mass transfer, the extent to which hyperpolarization is relayed into the particle interior depends on the Thiele modulus and effectiveness factor, as discussed above. For the specific cases of ϕ_S = 2.0 and 20, the effectiveness factor (η) is calculated to be 0.81 and 0.14, respectively, values which manifest the different mean dissipation rates (which depend on both spin-lattice relaxation and polarization level) of hyperpolarization in the interior relative to the surface. The enhancement of polarization in the solid can be related to the surface polarization by, $\varepsilon_{\theta,S} = \eta(\tilde{P}|_{\tilde{r}=1} - 1) + 1$, where $\tilde{P}|_{\tilde{r}=1}$ values for different conditions are indicated by the black points in Fig. 6a-c. Schematic polarization profiles are shown in Fig. 6a,b for a fixed Damköhler number of 0.02, and different values of the Thiele modulus. For ϕ_S = 2.0 (Fig. 6a), spin polarization in the DNP matrix *M* effectively hyperpolarizes the particle surface and polarization is able to penetrate significantly into the solid polystyrene target (the "sink" *S*), thereby hyperpolarizing the particle interior. By comparison, for ϕ_S = 20 (Fig. 6b), the solid particle surface is also effectively hyperpolarized, although the interior becomes polarized to a negligible extent, due to rapid spin-lattice relaxation within the particle. For conditions corresponding to a much larger Damköhler number of 500 and ϕ_S = 2.0 (Fig. 6c), a similarly negligible extent of polarization penetrates into the solid particle interior, in this case due to low transfer of polarization to the particle surface. In general, for large Da_P values (Da_P >>1), the hyperpolarization reservoir within the DNP matrix becomes depleted near particle surfaces, resulting in the formation of a depletion layer. Regardless, for ϕ_S = 2.0, the average dissipation rate of hyperpolarization within the interior relative to the, now diminished, surface polarization still corresponds to η = 0.81, as depicted schematically in the inset of Fig. 6c. For large Da_P conditions, DNP matrix-mediated spin-diffusion is an ineffective mechanism for polarizing solid-particle targets. While the solution to Eq. 9 and the effectiveness factor will have different functional forms depending on geometry of the system, both Da_P and ϕ_S depend solely on the material properties of the system and can be used to parametrize the efficacy of polarization transfer between two (or more) media that are coupled by spin diffusion. Such dimensional property analyses yield results that are consistent with those obtained by numerical simulations[24] and enable enhancement values to be predicted and rate-limiting polarization transfer processes to be identified by use of simple analytical relationships.

Direct versus spin-diffusion-mediated polarization transfer at surfaces

Although thermal-like boundary conditions[64] are generally justified for homogenous diamagnetic systems, heterogeneous systems require accounting for the different rates of hyperpolarization propagation and dissipation within the dissimilar media, as well as transfer across their mutual interfaces. Importantly, higher local concentrations of biradicals at the solvent-solid interface can significantly influence local polarization transfer processes. In general, the effects of such interfacial phenomena have been challenging to elucidate for composite spin systems, such as those exploited in hyperpolarized magnetic resonance[7,65] and for quantum interface control.[11,66] As schematically depicted in Fig. 1b, in DNP-NMR experiments, adsorbed or near-surface biradicals can directly polarize ^{1}H nuclei within the solid-particle interior up to the range of the hyperfine interaction. It is assumed that the solid is free of paramagnetic impurities, which could otherwise diminish the efficacy of DNP cross-effect transfer.[7] Due to the different local environment experienced by near-surface paramagnetic centers, their associated DNP source term ($\dot{Q}$) differs from those in the bulk DNP matrix, according to the Zeeman conductivity and spin-relaxation properties of the surface with which they are in contact. This interfacial region, *I*, may be approximated as an additional film resistance separating the two bulk media over the annulus $R>r>(R-\lambda_{ws,I})$, as depicted in Fig. 7a. Specifically, the Zeeman energy flux (W/m^2) into Region *I* due to direct DNP is represented by $\rho_{H,S}C_z k_{DNP}(\rho_{H,S})\Delta\tilde{P}$, such that the polarization build-up rate and signal gain over $R>r>(R-\lambda_{ws,I})$ can be calculated by the lumped-element approximation associated with Eqs. 5a, 6, and 7. The build-up rates and polarization gain are calculated to be $\varepsilon^0_{\theta,I}$=8.3, $\theta^0_{depo,I}$=0.97, and $T^0_{DNP,I}$=1.2 s for $k_{DNP}L^{-1}$ = 0.04 s^{-1} corresponding to 2 mM AMUPol ($\lambda_{ws,I}$= 5.8 nm) and polystyrene (ρ_H= 70 M). Due to the relatively short $T^0_{1,S}$ = 1.3 s of amorphous polystyrene, these interfacial ^{1}H nuclei retain polarization poorly compared to the DNP matrix. For this spin system, it can be determined from Eq. 9, that the near-surface radicals will exhibit a "spin Hatta effect," which yields an increased rate of polarization transfer relative to bulk radical species. Due to this increased rate of polarization transfer, at very early times ($t << T^0_{DNP,M}$) there will be an initial diffusive flux from Region *I* into Region *M*, which will revert as the polarization gradient is established. Direct hyperpolarization of the solid-particle surface enhances fast relaxing ^{1}H spins near the interface, resulting in faster build-up times both in the DNP matrix and in the bulk solid particle due to ^{1}H-^{1}H dipolar interactions. At steady-state, the measured DNP signal enhancement ($\varepsilon_{\infty,i}$) corresponds to the average polarization with, $\tilde{P}_i|_{on}$, and without, $\tilde{P}_i|_{off}$, microwave irradiation, $\varepsilon_{\infty,i} = 1/V_i \cdot \iiint(\tilde{P}_i|_{on}/\tilde{P}_i|_{off})dV_i$, which can be independently measured for each region for which distinct NMR signals are resolved.

Assuming that the DNP matrix is uniformly distributed around each solid particle, , Eq. 9, can be solved numerically to obtain spatial polarization profiles. For the conditions above, Fig. 7a shows a calculated plot of the steady-state ^{1}H signal enhancement ($\varepsilon_{\infty,i}$) profile within a 100-nm polystyrene particle, across the interfacial region, and within a thin 12-nm DNP-matrix layer. For the thin DNP-matrix layer, ^{1}H spin-lattice relaxation in the solid-particle sink significantly reduces polarization levels in the DNP matrix from the maximum value attainable for the homogeneous case, $\varepsilon^0_{\infty,M}$=230, to that calculated for this heterogeneous suspension, $\varepsilon_{\infty,M}$=7. As discussed above, polarization dissipation rates in the interior are characterized by the Thiele modulus in the solid-particle, $\phi_S \equiv R/(\mathcal{D}_{H,S}T^0_{1,S})^{0.5}$, where larger ϕ_S values correspond to stronger polarization sinks and diminished enhancements. In Fig. 7b, measured $\varepsilon^0_{\infty,M}$, $\varepsilon_{\infty,M}$, and $\varepsilon_{\infty,S}$ values are plotted versus matrix $\rho_{H,M}^{1/3}$ for polystyrene-DNP-matrix

suspensions, which elucidate both the contribution of direct DNP transfer to solid-particle surfaces and the utility of ϕ_S for predicting the extent to which a solid may be hyperpolarized. For longer ^{1}H spin-lattice relaxation times, $\phi_S \rightarrow 0$, and the DNP signal enhancement in the solid particle $\varepsilon_{\infty,S}$ approaches the maximum value attainable, namely that of the homogeneous DNP matrix $\varepsilon^0_{\infty,M}$ (Fig. 7b, ●). For the 100-nm polystyrene particles and conditions used here, ϕ_S=2.0, which establishes that the internal rate of dissipation of ^{1}H polarization by spin-lattice relaxation is twice the rate of ^{1}H spin diffusion, leading to significantly lower enhancements of both the polystyrene $\varepsilon_{\infty,S}$ (◆) and the DNP matrix $\varepsilon_{\infty,M}$ (×). For low $\rho_{H,M}$, the Zeeman conductivity ($\rho_H C_Z \mathcal{D}_H$) of the DNP matrix is too low to efficiently polarize the solid-particle surface by matrix-mediated ^{1}H spin diffusion alone. This corresponds to a large Damköhler number conditions and is analogous to thermal energy conduction between a low heat-capacity fluid and a high heat-capacity solid, the latter of which exhibits smaller changes in temperature. Deviation among $\varepsilon_{\infty,S}$ values from the analytical plot for ϕ_S=2.0 in Fig. 7b provides strong evidence that hyperfine-mediated polarization transfer to the solid-particle surface contributes significantly to hyperpolarization of composite spin systems. As reflected in the analytical plots for ϕ_S >0.1, the magnitude and rate of hyperpolarization transfer by DNP matrix-mediated spin-diffusion is often not sufficient to overcome thermally driven spin-lattice relaxation in the solid particle target. Instead, polarization transfer at low $\rho_{H,M}$ may be dominated by direct DNP transfer from near-surface radical species. Despite the complicated nature of the interface, noteworthy agreement is obtained between experiment and numerical solutions (solid-yellow line, Fig. 7b) that account for radical-surface interactions without adjustable parameters, under the conditions discussed above. Further evidence for such direct polarization transfer is provided by the nearly constant signal enhancement $\varepsilon_{\infty,M}$ (×) of the DNP matrix as a function of $\rho_{H,M}^{1/3}$ over the range of conditions examined. While energy transfer from the DNP matrix to the solid target is relatively poor when matrix ^{1}H densities $\rho_{H,M}$ are low, the ensemble of spins in the DNP matrix is nevertheless rapidly polarized to $\varepsilon_{\infty,M} \approx \varepsilon^0_{\theta,I}$ by dipolar contact with the solid target surface which often has a larger Zeeman spin conductivity (due to partial deuteration of the DNP matrix, $\rho_{H,S}\mathcal{D}_{H,S}C_Z >> \rho_{H,M}\mathcal{D}_{H,M}C_Z$). Consequently, the steady-state hyperpolarization levels that are established in the dipole-dipole-coupled spin ensembles of the DNP matrix and solid particles mutually depend on the relative rates of polarization generation, propagation, and dissipation in the respective media, in accordance with classical spin thermodynamics and the underlying quantum processes. The constitutive model thus yields quantitative understanding of the physical processes that account for the hyperpolarization levels that are measured experimentally, including the roles of interfacial interactions and non-equilibrium effects that are important in mesoscopic spin transport processes generally.

4. Conclusions

The dimensional scaling analyses presented here generalize aspects of spin polarization transfer phenomena across multiple length scales and across strong local magnetic field gradients. In particular, the utility of such scaling analyses are shown to quantitatively describe hyperpolarization transfer to surrounding nuclear spin ensembles, mediated by slow exchange across a quantum interface, specifically the spin-diffusion barrier. The resulting bulk constitutive model is directly analogous to the heat equation and provides a continuum description of hyperpolarization transfer in non-conducting solids containing dilute paramagnetic centers. The rate of excess Zeeman energy transfer (*i.e.*, DNP injection rate) from paramagnetic centers is proportional to the product $\rho_H C_Z k_{DNP}$, which is analogous to a heat transfer coefficient. Measurement of the DNP polarization transfer coefficient, k_{DNP}, enables distinct kinetic regimes associated with different rate-limiting polarization transfer processes to be distinguished. Quantitative experimental evidence supports the existence of an energy barrier that impedes polarization transfer near paramagnetic centers and which is crucially influenced by the local ^{1}H spin density. Although higher ^{1}H spin densities are desirable to maximize the flux of Zeeman energy into the bulk matrix, a kinetic limit is encountered at intermediate values of the ^{1}H spin density, after which the apparent rate of hyperpolarization transfer into the bulk matrix declines. This kinetically-limited regime is attributed to dissipative or transport processes that occur among hyperfine-coupled ^{1}H nuclei, which classically, can be generalized by using a spin polarization analogue of the Hatta number provided that spatially-dependent spin relaxation, polarization generation, and spin-diffusion rates are explicitly known. The film-transfer model in the "thermally thin" limit yields simple quantitative criteria (Eqs. 5a, 6, and 7) for optimizing cross-effect DNP conditions or other hyperpolarization transfer protocols. A more general conclusion is that the utility of hyperpolarization techniques could be significantly improved if kinetic limitations, such as the spin-diffusion barrier, were diminished. This motivates further development of new paramagnetic species, polarization conduction matrices, or electron-nuclear spin excitation methodologies to mitigate these kinetic factors, guided both by the dimensional property relationships presented here and by first-principles quantum mechanical calculations.

Far from paramagnetic centers, hyperpolarization transfer is shown to adhere to spin thermodynamic formalisms similar to thermal energy conduction processes. However, near the paramagnetic centers ($r < \lambda_{sdb}$) or in related phenomena involving polarization transfer between frequency-shifted nuclei (*e.g.*, nuclear spin waves[67,68]), such thermal-like conduction may not strictly apply and require modification, as presented here for the propagation of net nuclear magnetization, to obtain meaningful quantitative results. Lastly, interfacial phenomena, including adsorption of biradical polarizing agents, are shown to significantly influence polarization transfer kinetics between bulk reservoirs of nuclear spins. Despite these complexities, it is demonstrated that continuum analyses can provide important insights near quantum interfaces (*e.g.*, spin-diffusion barrier), as the Nernst-Planck equation does for dilute electrolyte systems. The DNP polarization transfer coefficient, as demonstrated here, is a useful concept to measure and compare polarization transfer rates in heterogeneous spin systems. Film coefficients are widely applied in heat and mass transfer, and, for the spin-diffusion barrier, further analogies may be extended to concepts in electrochemistry

such as the Debye length or the charge-transfer coefficient in the Butler-Volmer model.[69] In a broader context, these results provide a system-level description of complex composite spin systems. Such approaches may be used to guide the selection of material properties to optimize polarization transfer between dissimilar spin reservoirs which remains crucial to hyperpolarized magnetic resonance and quantum information applications. Similar scaling analyses are expected to yield system-level insights into spin-transfer phenomena in other condensed matter systems where transitions from quantum mechanical to classical properties feature prominently.

5. Materials and Methods

Sample preparation

DNP-NMR measurements were performed on a frozen biradical solution and on frozen polystyrene microparticle suspensions. Stock solutions containing 2 mM or 12 mM stable nitroxide biradical AMUPol (Cortecnet) were prepared by using glycerol/H_2O (60/40 vol%) and d_8-glycerol/D_2O (60/40 vol%). The partially deuterated solvents used in the MAS-DNP experiments were prepared by sequential dilution of the AMUPol glycerol/H_2O (60/40 vol%) solutions with aliquots of AMUPol d_8-glycerol/D_2O (60/40 vol%) solutions. Low-dispersity 0.1 ±0.01 µm polystyrene microbeads were acquired from Sigma-Aldrich, suspended in 99.99 atom% D_2O, and freeze-dried prior to use. For frozen biradical solutions, approximately 20 µL of each solution were injected into a 3.2 mm sapphire rotor, packed with a polytetrafluorethylene (PTFE) insert and capped with a zirconia MAS drive cap, and inserted into the pre-cooled spectrometer. For solid containing samples, approximately 13 mg of dry polystyrene particles were combined with 10 µL of DNP solution under incipient wetness conditions and were mixed by hand with a glass stir rod.

DNP-NMR measurements

Solid-state MAS-DNP measurements were conducted on a wide-bore 400 MHz (B_0 = 9.4 T) Bruker Avance IIIHD spectrometer equipped with 263 GHz gyrotron, a low-temperature cooling cabinet, and a triple-resonance (H-X-Y) 3.2 mm low-temperature MAS probe. The protocols for measuring T_1, T_{DNP}, ε_∞, ε_θ, and θ_{depo} values were similar to those described previously.[27,52] The ^{1}H spin-echo saturation recovery experiments were conducted at 12.5 kHz MAS and 100 K with a fixed echo delay of τ_r =80 µs, proton 90° and 180° pulses calibrated to a pulse power of 83.3 kHz, and with a saturation train of twenty 90°-pulses separated by a 20 ms delay. Each data point in Fig. 3a and Fig. 5 corresponds to a saturation recovery plot containing 10 to 20 time increments measured with microwave irradiation and with the signal intensity, $S_{on,i}(t)$, normalized with respect to the steady-state microwave off signal intensity:

$$S_{\mathrm{on},i}(t) = \varepsilon_{\infty,i} \cdot \left[1 - \exp\left(-{}^{t}/_{T_{\mathrm{DNP},i}}\right)\right]. \qquad (13)$$

corresponding to mono-exponential polarization build up kinetics. The characteristic time $T_{DNP,i}$ is similar both with, $T_{DNP(on),i}$, and without, $T_{DNP(off),i}$, microwave irradiation (see experimental values in Table S1 in S.I. Section S1). To determine depolarization factors (θ_{depo}) for frozen 2 mM AMUPol solutions shown in Fig. 5, quantitative single-pulse ^{1}H MAS NMR experiments were conducted at 12.5 kHz MAS and 100 K with background subtraction. The depolarization factor in the limit of dilute paramagnetic centers is given by:

$$\theta^0_{\mathrm{depo},i} = \frac{S_{\mathrm{off},i}(\text{with AMUPol})}{S_{\mathrm{off},i}(\text{without AMUPol})}\ , \qquad (14)$$

where $S_{off,i}$, the signal intensity in the absence of microwave irradiation, is compared with external frozen glycerol-water standards that do not contain biradical species. Meanwhile, at high concentrations of paramagnetic centers, it is necessary to perform static experiments to assess the influence of depolarization effects from paramagnetic quenching effects.

By a similar procedure, solid suspensions were measured by using ^{13}C-detected 1D ^{13}C{^{1}H} CP-MAS saturation recovery experiments with a CP contact time of 2 ms at 9.4 T, 11.5 kHz MAS, and 100 K. The ^{13}C-detected experiment is used to independently determine $\varepsilon_{\infty,M}$ and $\varepsilon_{\infty,S}$ values for glycerol and polystyrene, respectively, for the analyses in Fig. 7b. For dry polystyrene particles, a value of $T^0_{1,S}$ = 1.3 ±0.1 s was measured by 1D ^{13}C{^{1}H} CP-MAS saturation recovery experiments in the absence of a DNP matrix. Similarly, characteristic ^{1}H DNP build-up times for polystyrene, $T_{DNP,S}$, and glycerol, $T_{DNP,M}$, are measured by ^{13}C{^{1}H} CP-MAS saturation recovery (see experimental values in Table S2 in S.I. Section S1).

Analytical solutions

The analytical solutions to Eq. 9 used to generate the dashed lines in Fig. 7b assumes that the lumped-element approximation for the DNP source term, $\dot{Q}$, is valid and that direct hyperpolarization of the solid-particle by hyperfine interactions does not occur. Within the solid-target particle over $0 < r < R$, the spatial polarization profile is:

$$\tilde{P}_S(\tilde{r}) = 1 + \frac{(\tilde{P}_S|_{\tilde{r}=1} - 1)\sinh[\emptyset_S \tilde{r}]}{\tilde{r} \qquad \sinh[\emptyset_S]} \qquad (15)$$

and within the DNP matrix over $R < r < R+\Delta R_{eff}$ is:

$$\tilde{P}_M(\tilde{r}) = \Xi_M - \Gamma_I \frac{\frac{1}{3}\mathrm{Da_P}\,\eta\left(\tilde{P}_S|_{\tilde{r}=1} - 1\right)}{\sinh\left[\emptyset_M^*\right] - \Gamma_{II}\cosh\left[\emptyset_M^*\right]} \cdot \left(\frac{\sinh\left[\emptyset_M^*\tilde{r}\right]}{\tilde{r}} - \Gamma_{II}\frac{\cosh\left[\emptyset_M^*\tilde{r}\right]}{\tilde{r}}\right) \quad (16)$$

where $\tilde{r} = r/R$, $\emptyset_S$ is the Thiele modulus of the solid particle, and Ξ_M is $\varepsilon^{\mathrm{o}}_{\infty,M}$ or $\theta^{\mathrm{o}}_{\mathrm{depo},M}$ in the presence or absence of microwave irradiation determined from Eq. 6 or Eq. 7, respectively. Here, $\tilde{P}_S|_{\tilde{r}=1}$ corresponds to the surface polarization at the interface between the DNP matrix and solid-particle target,

$$\tilde{P}_S|_{\tilde{r}=1} = \frac{\Xi_M + \frac{\mathrm{Da_P}\eta}{3\Gamma_I}}{1 + \frac{\mathrm{Da_P}\eta}{3\Gamma_I}} \quad , \quad (17)$$

which demonstrates the utility of the Damköhler number, $\mathrm{Da_P}$, and effectiveness factor, η, in evaluating the efficacy of DNP matrix-mediated hyperpolarization transfer to an arbitrary solid-target. For evaluation of Eqs. 15-17, the effective Thiele modulus for the DNP matrix ($\emptyset_M^*$) is:

$$\emptyset_M^* = \emptyset_S \sqrt{\frac{\mathcal{D}_{\mathrm{H},S} T^{\mathrm{o}}_{1,S}}{\mathcal{D}_{\mathrm{H},M} T^{\mathrm{o}}_{\mathrm{DNP},M}}} \quad (18)$$

and geometry specific integration constants Γ_I and Γ_{II} corresponding to spherical 1D radial symmetry and thermal-like boundary conditions are:

$$\Gamma_I = -\frac{\tanh\left[\emptyset_M^*\right] - \Gamma_{II}}{\emptyset_M^* + \Gamma_{II} - \tanh\left[\emptyset_M^*\right](1 + \emptyset_M^*\Gamma_{II})} \quad , \quad (19)$$

$$\Gamma_{II} = \frac{(1 + \frac{\Delta R_{\mathrm{eff}}}{R})\emptyset_M^* - \tanh\left[(1 + \frac{\Delta R_{\mathrm{eff}}}{R})\emptyset_M^*\right]}{(1 + \frac{\Delta R_{\mathrm{eff}}}{R})\emptyset_M^* \tanh\left[(1 + \frac{\Delta R_{\mathrm{eff}}}{R})\emptyset_M^*\right] - 1} \quad , \quad (20)$$

where, in Eq. 18, $T^{\mathrm{o}}_{1,S}$ and $T^{\mathrm{o}}_{\mathrm{DNP},M}$ correspond to the spin-lattice relaxation time of the solid and characteristic build-up time of the DNP matrix respectively; these 'o' properties correspond to the individual components, not those of a matrix-particle suspension. The volumetric mean of the spatial polarization levels within the solid-particle target is:

$$< \tilde{P}_S > = \eta\left(\tilde{P}_S|_{\tilde{r}=1} - 1\right) + 1 \quad , \quad (21)$$

which corresponds to the solid-enhancement, $\varepsilon_{\theta,S} \equiv < \tilde{P}_{S(\mathrm{on})} >$, or depolarization factor, $\theta_{\mathrm{depo},S} \equiv < \tilde{P}_{S(\mathrm{off})} >$, in the presence or absence of microwave irradiation respectively. Importantly, the commonly reported signal enhancement is given, $\varepsilon_{\infty,S} \approx \varepsilon_{\theta,S}/\theta_{\mathrm{depo},S}$, for dilute ρ_{pc} where paramagnetic quenching is negligible. The dashed-lines in Fig. 7b correspond to these $\varepsilon_{\infty,S}$ values evaluated as a function of solvent and for $\emptyset_S$ values ranging from 0 to 2 to illustrate the influence of an increasingly strong solid-particle polarization sink. These expressions are useful in conceptualizing hyperpolarization transfer in composite systems but have limited utility considering the importance of radical-surface interactions in most systems. Similar analytical solutions to Eq. 9 accounting for radical-surface interactions may be developed, however numerical solutions are preferable. Importantly, without invoking the polarization-transfer coefficient, k_{DNP}, and effective polarization-level generated by cross-effect DNP, $\overline{P}_{\mathrm{CE}}$, description of polarization transfer processes in composite systems would likely be analytically intractable. More detailed derivations of the analytical solutions presented in this work is provided in the SI.

Numerical simulations

Numerical solutions to Eq. 9 corresponding to the solid-line plotted in Fig. 7b in the main text were obtained using the Matlab™ *pdepe* solver function assuming 1D spherical symmetry for the specified conditions similar to that described previously[24]. All hyperpolarization generation, propagation, and relaxation rates were estimated analytically by the lumped-element approximation. Assuming negligible agglomeration and that the frozen homogeneous DNP solvent is uniformly distributed among the 100-nm particles, a solvent-solid ratio of ~1.3 mg/μL corresponds to an effective solvent shell thickness of ΔR_{eff} ~12 nm for spherically smooth polystyrene particles.

Conflicts of interest

There are no conflicts to declare.

Acknowledgements

The authors thank B.J. Walder and T.C. Farmer for helpful discussions regarding nuclear spin diffusion and scaling analyses, respectively. Funding was provided in part by the USARO under contract W911NF-09-D-0001 via the Institute for Collaborative Biotechnologies, by the MRSEC program of the U.S. National Science Foundation under award no. DMR 1720256 (a www.mrfn.org), and by the Swiss National Science Foundation via grant no. 200020_178860.

Notes and references

1 W. G. Whitman and J. L. Keats, *Ind. Eng. Chem.*, 1922, **14**, 186–191.
2 E. M. Purcell, *Am. J. Phys.*, 1977, **45**, 3–11.
3 S. J. Nelson, J. Kurhanewicz, D. B. Vigneron, P. E. Z. Larson, A. L. Harzstark, M. Ferrone, M. van Criekinge, J. W. Chang, R. Bok, I. Park, et al., *Sci. Transl. Med.*, 2013, **5**, 198ra108.
4 Y. Lee, G. S. Heo, H. Zeng, K. L. Wooley and C. Hilty, *J. Am. Chem. Soc.*, 2013, **135**, 4636–4639.
5 T. Theis, G. X. Ortiz, A. W. J. Logan, K. E. Claytor, Y. Feng, W. P. Huhn, V. Blum, S. J. Malcolmson, E. Y. Chekmenev, Q. Wang and W. S. Warren, *Sci. Adv.*, 2016, **2**, 1–8.
6 M. Cavaillès, A. Bornet, X. Jaurand, B. Vuichoud, D. Baudouin, M. Baudin, L. Veyre, G. Bodenhausen, J. N. Dumez, S. Jannin, C. Copéret and C. Thieuleux, *Angew. Chemie - Int. Ed.*, 2018, **57**, 7453–7457.
7 P. R. Zangara, J. Henshaw, D. Pagliero, A. Ajoy, J. A. Reimer, A. Pines and C. A. Meriles, *Nano Lett.*, 2019, **19**, 2389–2396.
8 Y. Shiomi, J. Lustikova, S. Watanabe, D. Hirobe, S. Takahashi and E. Saitoh, *Nat. Phys.*, 2019, **15**, 22–26.
9 G. Kurizki, P. Bertet, Y. Kubo, K. Mølmer, D. Petrosyan, P. Rabl and J. Schmiedmayer, *Proc. Natl. Acad. Sci. U. S. A.*, 2015, **112**, 3866–3873.
10 V. Ranjan, G. de Lange, R. Schutjens, T. Debelhoir, J. P. Groen, D. Szombati, D. J. Thoen, T. M. Klapwijk, R. Hanson and L. Dicarlo, *Phys. Rev. Lett.*, 2013, **110**, 067004.
11 D. A. Gangloff, G. Éthier-Majcher, C. Lang, E. V. Denning, J. H. Bodey, D. M. Jackson, E. Clarke, M. Hugues, C. Le Gall and M. Atatüre, *Science*, 2019, **364**, 62–66.
12 A. S. Lilly Thankamony, J. J. Wittmann, M. Kaushik and B. Corzilius, *Prog. Nucl. Magn. Reson. Spectrosc.*, 2017, **102–103**, 120–195.
13 A. Karabanov, D. Wiśniewski, I. Lesanovsky and W. Köckenberger, *Phys. Rev. Lett.*, 2015, **115**, 1–5.
14 G. Sharma, T. Gaebel, E. Rej, D. J. Reilly, S. E. Economou and E. Barnes, *Phys. Rev. B*, 2019, **205423**, 1–12.
15 K. O. Tan, M. Mardini, C. Yang, J. H. Ardenkjær-Larsen and R. G. Griffin, *Sci. Adv.*, 2019, **5**, eaax2743.
16 C. Ramanathan, *Appl. Magn. Reson.*, 2008, **34**, 409–421.
17 J. J. Wittmann, M. Eckardt, W. Harneit and B. Corzilius, *Phys. Chem. Chem. Phys.*, 2018, **20**, 11418–11429.
18 F. A. Perras, M. Raju, S. L. Carnahan, A. C. T. Van Duin, A. J. Rossini and M. Pruski, *J. Phys. Chem. Lett.*, 2020, **11**, 5655–5660.
19 K. R. Thurber and R. Tycko, *J. Chem. Phys.*, 2012, **137**, 084508.
20 F. Mentink-Vigier, *Phys. Chem. Chem. Phys.*, 2020, **22**, 3643–3652.
21 K. L. Ivanov, A. N. Pravdivtsev, A. V. Yurkovskaya, H. M. Vieth and R. Kaptein, *Prog. Nucl. Magn. Reson. Spectrosc.*, 2014, **81**, 1–36.
22 F. A. Perras and M. Pruski, *J. Chem. Phys.*, 2018, **149**, 154202.
23 F. Mentink-Vigier, S. Vega and G. De Paëpe, *Phys. Chem. Chem. Phys.*, 2017, **19**, 3506–3522.
24 A. Pinon, J. Schlagnitweit, P. Berruyer, A. Rossini, M. Lelli, E. Socie, M. Tang, T. Pham, A. Lesage and L. Emsley, *J. Phys. Chem. C*, 2017, **121**, 15993–16005.
25 A. A. Smith, B. Corzilius, A. B. Barnes, T. Maly and R. G. Griffin, *J. Chem. Phys.*, 2012, **136**, 015101.
26 B. Corzilius, A. A. Smith and R. G. Griffin, *J. Chem. Phys.*, 2012, **137**, 054201.
27 A. Leavesley, S. K. Jain, I. Kaminker, H. Zhang, S. Rajca, A. Rajca and S. Han, *Phys. Chem. Chem. Phys.*, 2018, **20**, 27646.
28 A. Z. Genack and A. G. Redfield, *Phys. Rev. Lett.*, 1973, **31**, 1204–1207.
29 N. Bloembergen, *Physica*, 1949, **15**, 386–426.
30 A. Abragam, *The Principles of Nuclear Magnetism*, Oxford University Press, 1961.
31 P. G. de Gennes, *J. Phys. Chem. Solids*, 1958, **7**, 345–350.
32 A. E. Dementyev, D. G. Cory and C. Ramanathan, *Phys. Rev. B - Condens. Matter Mater. Phys.*, 2008, **77**, 1–5.
33 G.R. Khutsishvili, *Usp. Fiz. Nauk*, 1965, **87**, 211–254.
34 Q. Chen and K. Schmidt-Rohr, *Solid State Nucl. Magn. Reson.*, 2006, **29**, 142–152.

35 B. J. Walder, N. A. Prisco, F. M. Paruzzo, J. R. Yarava, B. F. Chmelka and L. Emsley, *J. Phys. Chem. Lett.*, 2019, **10**, 5064–5069.
36 A. C. Pinon, PhD thesis, École Polytechnique Fédérale de Lausanne, Switzerland, 2018.
37 M. E. Halse, A. Zagdoun, J. N. Dumez and L. Emsley, *J. Magn. Reson.*, 2015, **254**, 48–55.
38 A. A. Lee, C. S. Perez-Martinez, A. M. Smith and S. Perkin, *Phys. Rev. Lett.*, 2017, **119**, 1–5.
39 G. R. Khutsishvili, *Sov. Phys. JETP-USSR*, 1957, **4**, 382–384.
40 M. Goldman, *Phys. Rev.*, 1965, **138**, 1675–1681.
41 C. Sauvée, M. Rosay, G. Casano, F. Aussenac, R. T. Weber, O. Ouari and P. Tordo, *Angew. Chemie - Int. Ed.*, 2013, **52**, 10858–10861.
42 D. J. Kubicki, G. Casano, M. Schwarzwälder, S. Abel, C. Sauvée, K. Ganesan, M. Yulikov, A. J. Rossini, G. Jeschke, C. Copéret, A. Lesage, P. Tordo, O. Ouari and L. Emsley, *Chem. Sci.*, 2016, **7**, 550–558.
43 D. Mance, P. Gast, M. Huber, M. Baldus and K. L. Ivanov, *J. Chem. Phys.*, 2015, **142**, 234201.
44 D. J. Kubicki, A. J. Rossini, A. Purea, A. Zagdoun, O. Ouari, P. Tordo, F. Engelke, A. Lesage and L. Emsley, *J. Am. Chem. Soc.*, 2014, **136**, 15711–15718.
45 W. G. Whitman, *Int. J. Heat Mass Transf.*, 1962, **5**, 429–433.
46 W. Nernst, *Zeit. Phys. Chem.*, 1904, **47**, 52–55.
47 P. V. Danckwerts, *Chem. Eng. Sci.*, 1953, **2**, 1–13.
48 D. Peaceman, PhD thesis, Massachusetts Institute of Technology, 1951.
49 H. S. Carslaw and J. C. Jaeger, *Conduction of Heat in Solids*, Oxford Science Publications, 2nd edn., 1959.
50 D. W. van Krevelen and P. J. Hoftijzer, *Recl. des Trav. Chim. des Pays-Bas*, 1948, **67**, 563–586.
51 T. Sugishita, Y. Matsuki and T. Fujiwara, *Solid State Nucl. Magn. Reson.*, 2019, **99**, 20–26.
52 A. J. Rossini, A. Zagdoun, M. Lelli, D. Gajan, F. Rascón, M. Rosay, W. E. Maas, C. Copéret, A. Lesage and L. Emsley, *Chem. Sci.*, 2012, **3**, 108–115.
53 F. Mentink-Vigier, S. Paul, D. Lee, A. Feintuch, S. Hediger, S. Vega and G. De Paepe, *Phys. Chem. Chem. Phys.*, 2015, **17**, 21824 - 21836.
54 K. R. Thurber and R. Tycko, *J. Chem. Phys.*, 2014, **140**, 184201.
55 K. K. Frederick, V. K. Michaelis, M. A. Caporini, L. B. Andreas, G. T. Debelouchina, R. G. Griffin and S. Lindquist, *Proc. Natl. Acad. Sci. U. S. A.*, 2017, **114**, 3642–3647.
56 A. Zagdoun, G. Casano, O. Ouari, M. Schwarzwälder, A. J. Rossini, F. Aussenac, M. Yulikov, G. Jeschke, C. Copéret, A. Lesage, P. Tordo and L. Emsley, *J. Am. Chem. Soc.*, 2013, **135**, 12790–12797.
57 B. Corzilius, L. B. Andreas, A. A. Smith, Q. Z. Ni and R. G. Griffin, *J. Magn. Reson.*, 2014, **240**, 113–123.
58 S. Lange, A. H. Linden, Ü. Akbey, W. Trent Franks, N. M. Loening, B. J. Van Rossum and H. Oschkinat, *J. Magn. Reson.*, 2012, **216**, 209–212.
59 A. J. Rossini, A. Zagdoun, F. Hegner, M. Schwarzwälder, D. Gajan, C. Copéret, A. Lesage and L. Emsley, *J. Am. Chem. Soc.*, 2012, **134**, 16899–16908.
60 J. Schlagnitweit, M. Tang, M. Baias, S. Richardson, S. Schantz and L. Emsley, *J. Am. Chem. Soc.*, 2015, **137**, 12482–12485.
61 J. K. Nørskov, T. Bligaard, B. Hvolbæk, F. Abild-Pedersen, I. Chorkendorff and C. H. Christensen, *Chem. Soc. Rev.*, 2008, **37**, 2163–2171.
62 F. Mentink-Vigier, Ü. Akbey, H. Oschkinat, S. Vega and A. Feintuch, *J. Magn. Reson.*, 2015, **258**, 102–120.
63 F. A. Perras, R. R. Reinig, I. I. Slowing, A. D. Sadow and M. Pruski, *Phys. Chem. Chem. Phys.*, 2016, **18**, 65–69.
64 J. Clauss, K. Schmidt-Rohr and H. W. Spiess, *Acta Polym.*, 1993, **44**, 1–17.
65 F. A. Perras, L. L. Wang, J. S. Manzano, U. Chaudhary, N. N. Opembe, D. D. Johnson, I. I. Slowing and M. Pruski, *Curr. Opin. Colloid Interface Sci.*, 2018, **33**, 9–18.
66 J. O. Tenorio-Pearl, E. D. Herbschleb, S. Fleming, C. Creatore, S. Oda, W. I. Milne and A. W. Chin, *Nat. Mater.*, 2017, **16**, 208–213.
67 P. G. de Gennes, P. A. Pincus, F. Hartnam-Boutron, and J.M. Winter. *Phys. Rev.*, 1963, **129**, 1105–1115.
68 C. K. A. Mewes, *Nat. Phys.*, 2019, **15**, 8–9.
69 C. Lin, E. Laborda, C. Batchelor-Mcauley and R. G. Compton, *Phys. Chem. Chem. Phys.*, 2016, **18**, 9829–9837.

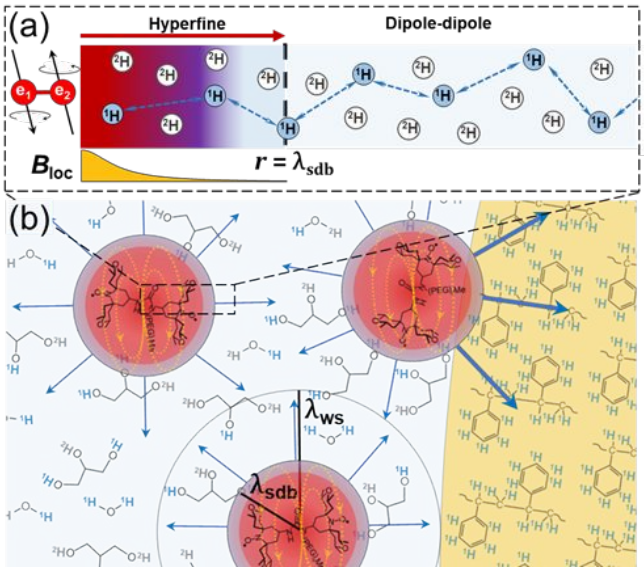

FIG 1. Schematic diagrams of (a) a spin-diffusion barrier and, (b) polarization transfer from paramagnetic centers in a partially deuterated glycerol-water matrix to a polymeric solid. Each biradical molecule is assumed to polarize a spherical region represented by the Wigner-Seitz radius, $\lambda_{\mathrm{ws}} = (3/4\pi\rho_{\mathrm{pc}}N_A)^{1/3}$ where ρ_{pc} is the biradical concentration.[24] The interface between the spin-diffusion barrier and the bulk diamagnetic matrix occurs at λ_{sdb}, and the mean biradical separation is $2\lambda_{\mathrm{ws}}$.

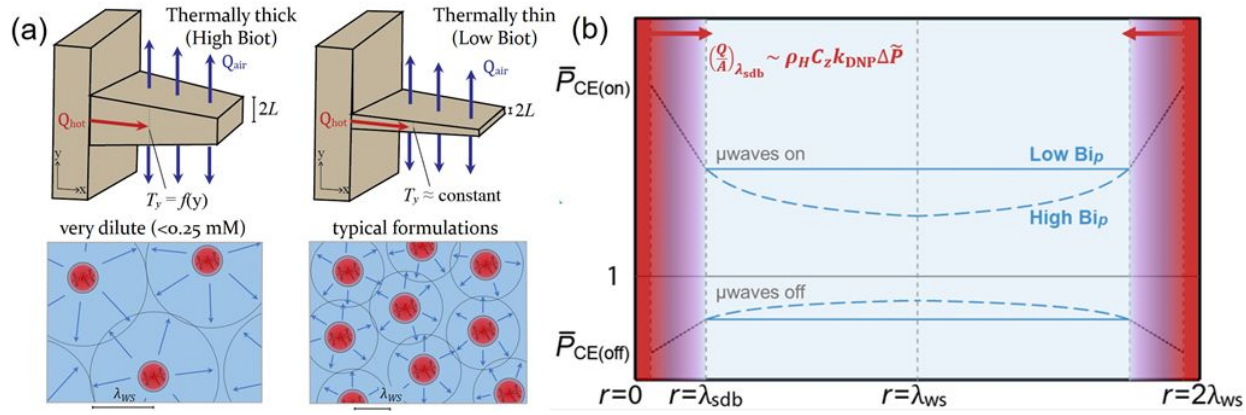

FIG 2. (a) Comparison of thermally thick versus thermally thin cooling fins and their analogies to bulk polarization transfer in very dilute (<0.25 mM) versus dilute (*e.g.*, 1-16 mM) biradical concentrations in frozen DNP matrices. (b) Schematic steady-state polarization profiles, $\tilde{P}(r)$, between two biradical species in a frozen DNP matrix with ($\overline{P}_{\mathrm{CE(on)}}$) or without ($\overline{P}_{\mathrm{CE(off)}}$) microwave excitation. For low $\mathrm{Bi_P}$ conditions (<0.65), the diamagnetic bulk approaches a nearly uniform polarization level (upper solid line), whereas for high $\mathrm{Bi_P}$ conditions (>0.65), a polarization gradient exists (upper dashed line). Thermal equilibrium corresponds to unity. The film-transfer model assumes a linear polarization gradient across the spin-diffusion barrier.

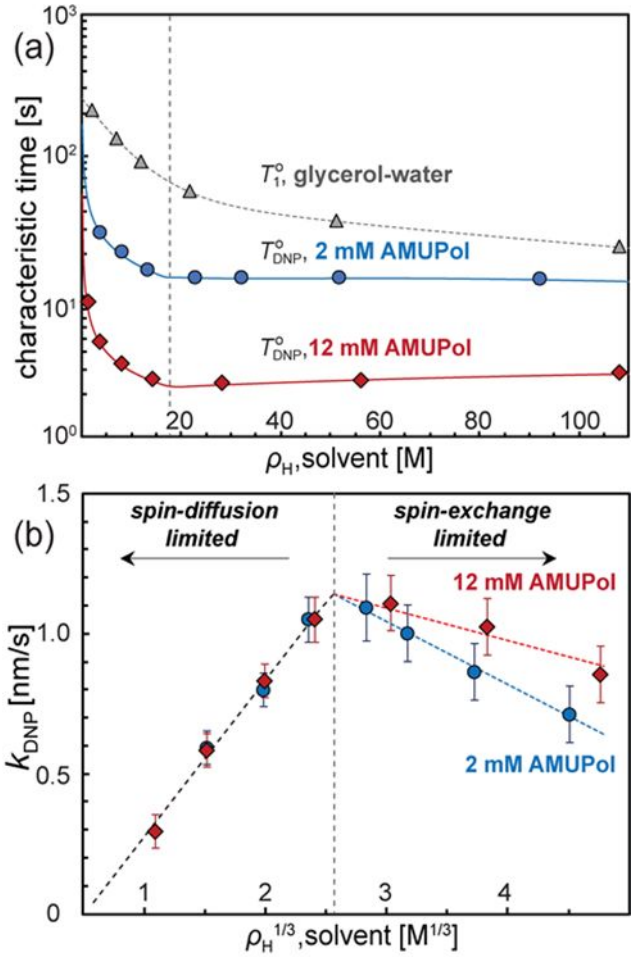

FIG 3. (a) Characteristic times T_1^o or T_{DNP}^o measured by ^{1}H spin-echo saturation recovery at 12.5 kHz MAS, 9.4 T, and 100 K for frozen glycerol-water matrices with different ^{1}H densities ρ_H and different concentrations of paramagnetic centers: without biradical (▲), with 2 mM (●) or 12 mM (◆) AMUPol; (b) k_{DNP} values as functions of $\rho_H^{1/3}$. Solid lines in (a) are from Eq. (4) using measured or fitted values for T_1^o and k_{DNP}.

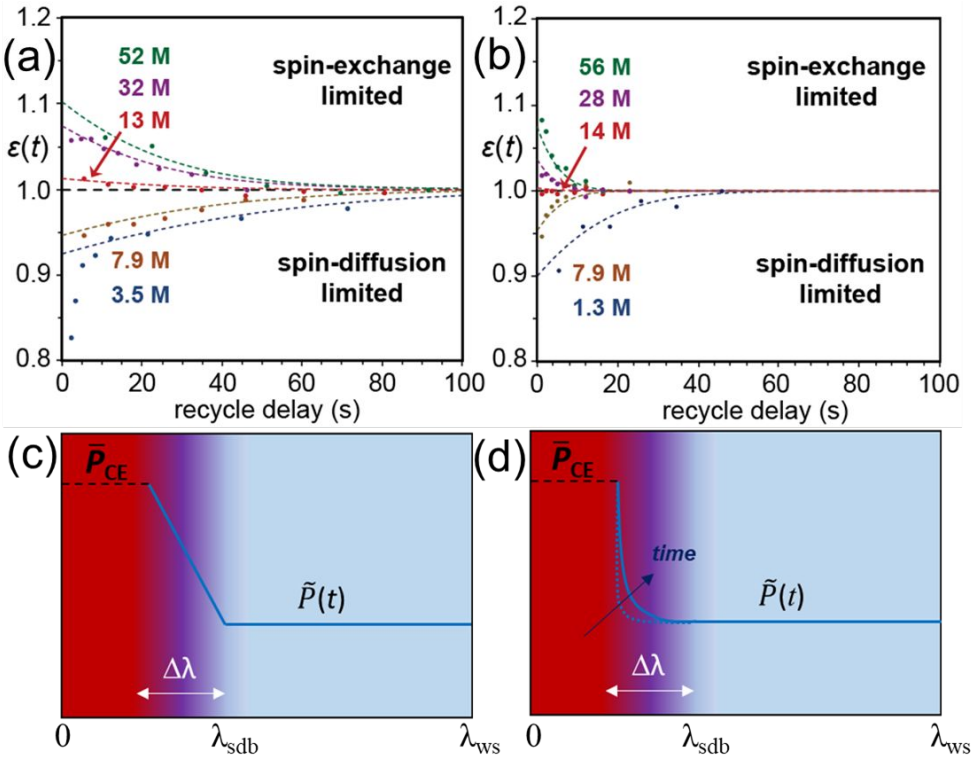

FIG 4. Normalized transient signal enhancement, $\varepsilon(t)$, plotted as functions of the recycle delay for (a) 2 mM AMUPol and (b) 12 mM AMUPol in glycerol-water for different ^{1}H concentrations in the frozen DNP matrix. In both (a) and (b), a crossover point occurs at $\rho_H \approx 13$ M, similar to that observed in Fig. 3b. Schematic diagrams of the polarization profiles across a spin-diffusion barrier predicted by film theory (c) without accounting for spin-lattice relaxation and (d) taking spin-lattice relaxation into account within the barrier. The profile in (c) is expected to more closely resemble a spin-diffusion-limited regime, and (d) a spin-exchange limited regime; note that (c) is not expected to be linear when surface curvature or spin-lattice relaxation are non-negligible.

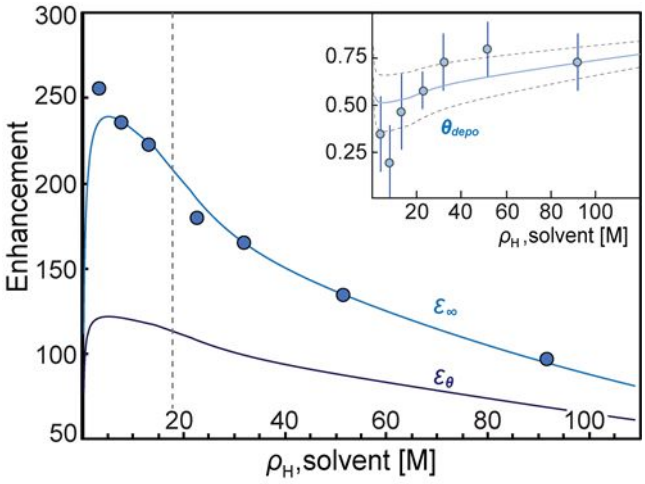

FIG 5. Steady-state NMR signal enhancements ε_∞^0 (inset: depolarization factors θ_{depo}^0) and $\varepsilon_\theta^0=\varepsilon_\infty^0\theta_{\mathrm{depo}}^0$ versus ρ_H for frozen 2 mM AMUPol glycerol-water measured by ^{1}H spin-echo saturation recovery at 12.5 kHz MAS, 9.4 T, and 100 K. Solid lines are from Eqs. 6 and 7 using measured or fitted values for T_1^0, k_{DNP}, and $\overline{P}_{\mathrm{CE}}$.

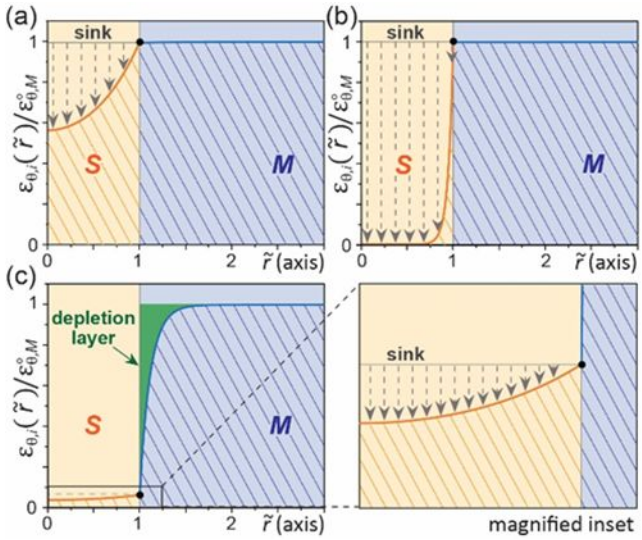

FIG 6. Normalized steady-state spatial polarization gain for conditions corresponding to (a) $Da_P = 0.02$ and $\phi_S = 2.0$, (b) $Da_P = 0.02$ and $\phi_S = 20$, and (c) $Da_P = 500$ and $\phi_S = 2.0$. Plots were generated using the analytical solution in Eq. 8.

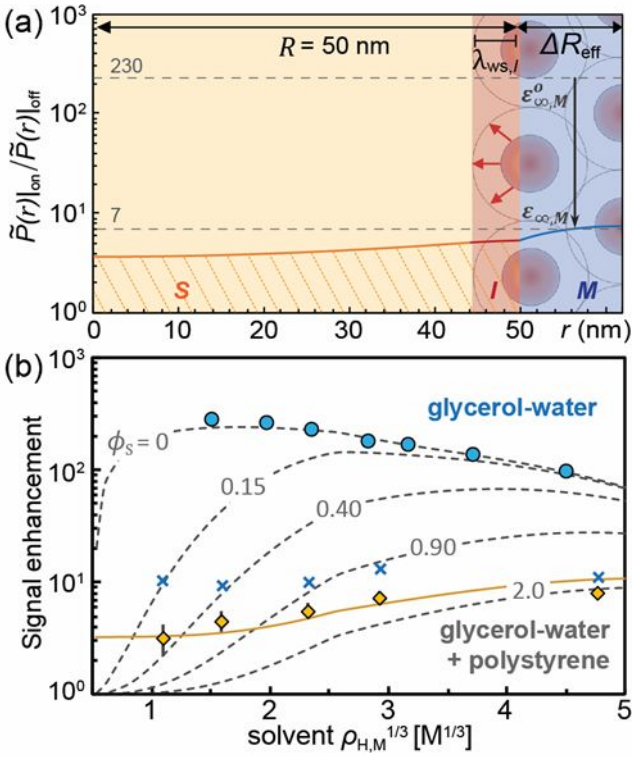

FIG 7. (a) Calculated steady-state ^{1}H polarization profile as a function of position r from the center of a 100-nm polystyrene sphere, surrounded by a 12-nm (ΔR_{eff}, solvent-solid ratio 1.3 µL/mg) frozen glycerol-water matrix ($\rho_{H,M}$=12 M) containing 2 mM AMUPol. (b) Measured enhancements $\varepsilon_{\infty,S}$ (◆) and $\varepsilon_{\infty,M}$ (✕) for the polystyrene particle suspension, compared to the DNP matrix $\varepsilon^0_{\infty,M}$ (●, Fig. 5). Dashed grey lines correspond to analytical solutions for $\varepsilon_{\infty,S}(\phi_S)$ for 0<ϕ_S<2 (neglecting biradical-surface interactions); solid yellow line accounts for biradical-surface interactions with ϕ_S=2.